In-phase electrodynamics and terahertz wave emission in extended intrinsic Josephson junctions

doi: 10.1103/PhysRevB.79.104522

In-phase electrodynamics and terahertz wave emission in extended intrinsic Josephson junctions

Tomio Koyama,[1,2,*] Hideki Matsumoto,[1,3,2,†] Masahiko Machida,[4,2,‡] and Kazuo Kadowaki[5,2,§]
[1]*Institute for Materials Research, Tohoku University, Sendai, 980-8577 Japan*
[2]*CREST(JST), 4-1-8 Honcho, Kawaguchi, Saitama 332-0012, Japan*
[3]*Department of Physics, Graduate School of Science, Tohoku University, Sendai 980-8574, Japan*
[4]*Center for Computational Science and e-Systems, Japan Atomic Energy Agency, 6-9-3 Higashi-Ueno, Taito-ku, Tokyo 110-0015, Japan*
[5]*Institute of Material Science, University of Tsukuba, Tsukuba, Ibaraki 305-8577, Japan*
(Received 30 November 2008; revised manuscript received 1 February 2009; published 31 March 2009)

Strong emission of subterahertz electromagnetic (EM) waves has been observed recently in the high T_c superconductor $Bi_2Sr_2CaCu_2O_8$ intrinsic Josephson junctions (IJJ's). We investigate numerically the dynamics of the EM fields both inside and outside the IJJ's emitting terahertz EM waves under a constant bias current, using two-dimensional models composed of IJJ's and the space surrounding them: (1) *xy* model and (2) *xz* model. In the *xy* model we investigate the EM modes excited in the *rectangular* junctions. In the voltage state the Josephson oscillation generates the oscillating EM field having nodes inside the junctions. The number of nodes depends on the DC voltage appearing in the junctions, and their direction is parallel to the shorter side of the junctions. The EM field shows a complex distribution pattern in the near field region. In the region far from the junctions we have only the expanding EM wave oscillating with the Josephson frequency. In the *xz* model we study the EM waves emitted in the *xz* plane from the junctions covered with normal electrodes. It is shown that the power of the emitted EM waves has distribution similar to that in the dipole emission in the system where electrodes of the same size are attached on top and bottom junctions. In the asymmetric system where the lower electrode is larger than the upper one the power distribution of emitted EM wave deviates from that in the dipole emission.

DOI: 10.1103/PhysRevB.79.104522 PACS number(s): 74.50.+r, 85.25.Cp

I. INTRODUCTION

Low energy *c*-axis electromagnetic (EM) properties of high T_c superconductors are well described by the intrinsic multi-Josephson junction model.[1] For example, the model explained successfully[2,3] the multiple branch structure of the *I-V* characteristics observed in $Bi_2Sr_2CaCu_2O_8$ (BSCCO).[4,5] Since the Josephson plasma frequencies of high T_c cuprates range from subterahertz to 10 terahertz region, which lie in the *terahertz gap* region, the possibility of the terahertz EM wave emission from intrinsic Josephson junctions (IJJ's) has been discussed for a long time, more than a decade by various authors.[6–17] As a mechanism that induces terahertz emission, the use of Josephson-vortex flow was proposed first in Ref. 7, and some indications of the emission in the presence of an applied magnetic field were reported in Refs. 14, 16, and 17. It was also reported that the emission from the nonequilibrium state in GHz region was observed without a magnetic field in BSCCO.[15]

Recently, Ozyuzer *et al.*[18] succeeded in observing directly the strong emission of terahertz electromagnetic waves in mesa-shaped samples of the high-temperature superconductor BSCCO IJJ's without an applied magnetic field. Their experimental results[18] are summarized as follows. (1) The mesa samples have an in-plane area of $\sim 300\ \mu m \times (40–100)\ \mu m$ and a thickness of $\sim 1\ \mu m$; that is, the in-plane dimensions are on the order of λ_c, the *c*-axis magnetic penetration depth, which is the length scale of the transverse Josephson plasma, and the mesas contain 6–700 intrinsic junctions. (2) The strong emission is observed first near the unstable point of the retrapping current in the uniform voltage branch when the bias current is decreased below the critical current I_c. (3) The emission is also observed in the other branches when the bias current is further decreased below the transition points to lower branches. In this case the power of emitted electromagnetic waves is proportional to N^2, N being the number of junctions in the voltage state, indicating that the coherent emission takes place. (4) The emitted EM waves are highly monochromatic ones. (5) The emitted power is $\sim 0.5\ \mu W$, which is much stronger compared with the emission from the single-junction systems ($\sim$pW).[19,20]

The possibility of the EM wave emission without an applied magnetic field was theoretically discussed in Ref. 13 on the basis of a linearized equation in which the amplitude of the spatial modulation of the phase differences is assumed to be small. However, in their calculations the emission from samples with small in-plane size of a few μm is considered, which is not the case of the experiment. In our previous papers,[21,22] we showed theoretically that the strong emission of monochromatic EM waves from the IJJ's is possible near the retrapping region in the *I-V* characteristics, which originates from the in-phase motion of the phase differences that is resonantly excited by the Josephson oscillations, and we calculated the voltage dependence of the emitted power. In the calculations, using a one-dimensional (1D) junction model with the dynamical boundary condition, we clarified the EM wave modes that are excited by the oscillating Josephson current and are emitted to outside the junctions. In the 1D junction systems there exist two kinds of oscillatory modes, depending on the length of the junctions, L. In the shorter junction systems satisfying $L < 3\lambda_c$ we found that monochromatic standing-wave modes can be excited, whose eigenfrequencies coincide with the Josephson frequencies at the dc voltage appearing in the junction. The emitted power in this case gradually increases with decreasing the induced voltage and takes a maximum value at the voltage corresponding to the retrapping current. In the longer junction

systems of $L \geq 3\lambda_c$, solitonic modes (or vortex-antivortex excitations) are excited at resonant frequencies depending on the length L, and the emitted power shows a sharp peak structure in these states. However, the eigenfrequency of the fundamental mode in the solitonic states is equal to half the Josephson frequency, not the Josephson frequency. These solitonic excitations are essentially the same as that coming from the resonance known as the *parametric excitation* in 1D long Josephson junctions.[23] Experimentally, the strong emission is observed in narrow voltage regions, and the frequency of the emitted EM wave corresponding to the fundamental mode is equal to the Josephson frequency.[18] This result indicates that the observed emission from the BSCCO IJJ's originates from the standing-wave modes. In our previous papers we also pointed out that the existence of an out-of-phase component of the phase differences contributes to make the resonance sharper even in the systems of $L \leq 3\lambda_c$.[22] The sharpness of the emission window thus might come from the contribution of an out-of-phase component of the phase differences existing in the multijunction systems.

There is a controversy about the excited EM modes which bring about the strong EM wave emission from the IJJ's. The calculations given in Refs. 24 and 25 claim that the EM modes excited in the IJJ's under a dc bias current include solitonic or vortexlike components arranged periodically along the c axis even in the absence of an external magnetic field and that the in-phase ac electric-field component relevant to the emission, which is superposed on the solitonic components, has a spatially *antisymmetric* pattern; i.e., $E_z(-x,t)=-E_z(x,t)$ (the magnetic field is *symmetric* in this case). Such an antisymmetric pattern of the electric field is similar to that appearing in an open cavity as is well known in the antenna theory.[26,27] On the other hand, the analysis given in Refs. 21 and 22 leads to an oscillating electric field having spatially symmetric distribution, i.e., $E_z(-x,t)=E_z(x,t)$ (the magnetic field is antisymmetric), which is analogous to the ac electric field inside a capacitor.[28] Since the pattern of emitted EM waves should depend on the excited EM field inside the IJJ's, the EM modes relevant to the emission will be checked experimentally by measuring the power distribution of the emitted EM waves. It is important to clarify the excited EM modes leading to the THz emission for establishing the physics of THz emission in IJJ's and also for devise applications. Hence, in this paper we developed a numerical method by which the EM field outside the IJJ's can be calculated unambiguously.

In this paper we present a numerical method for calculating the EM excitations in IJJ's and the emitted THz waves simultaneously. We use two simplified models composed of both IJJ's and the outside space, which will be called hereafter (a) the xy model and (b) the xz model, respectively. In these models the EM wave emission is described by solving the Maxwell equations numerically in both regions inside and outside the IJJ's under the conventional boundary condition for EM field at the junction edges, i.e., in which the EM field is continuous at boundaries. The xy model describes the in-phase EM excitations in a stack of infinite number of *rectangular* Josephson junctions. On the basis of this model we clarify the eigenmodes of the two-dimensional (2D) extended Josephson junctions. The effects of electrodes attached on the top and bottom junctions are also analyzed, using the xz model. These two models are solved under a constant bias current. The temporal and spatial variations in the phase differences and the EM fields are obtained in both regions inside and outside the IJJ's simultaneously. From the calculations for the xz model we show that the distribution of the emitted EM field is similar to that in the dipole emission. In the xy model we see that flux loops, which oscillate with the Josephson frequency, are formed inside the IJJ's along with nodes in between them, which are parallel to the shorter side of the rectangular junctions. The excited EM field is very much different from the solitonic (or parametric) excitations in 1D junctions; that is, the excitation modes of IJJ's composed of extended junctions are shown to be different from those in the 1D case in the absence of an external magnetic field.[21,22]

In Sec. II we first construct a set of coupled differential equations in the entire three-dimensional (3D) space including the vacuum outside the IJJ's on the basis of the Maxwell equations and the generalized Josephson relations. Then, the coupled equations used in the analysis of the xy and xz models are derived. In Sec. III, we explain the simulation method. To obtain correct behavior of the emitted EM waves we introduce the *perfectly matched layer*[29] (PML) in our simulation. The numerical results for the EM field are presented in Sec. IV. The spatial distributions of the EM field excited inside the junction are analyzed in various cases. The bias current dependence of the power of emitted EM waves is also clarified. Sec. V is devoted to the concluding remarks.

II. EQUATIONS FOR THE INTRINSIC JOSEPHSON JUNCTIONS

A. Three-dimensional model

Single crystals of BSCCO in which the superconducting CuO_2 layers and the insulating Bi-Sr-O layers are alternately stacked along the c axis form a stack of intrinsic Josephson junctions. The dynamics of the superconducting phase differences is well described by the multi-Josephson junction model composed of a stack of superconducting and insulating layers with thicknesses, respectively, $s \sim 3$ Å and $d \sim 12$ Å in which the junctions are capacitively and inductively coupled.

Consider the IJJ's with an in-plane area $L_x \times L_y$ and a thickness L_z. Here, we take the z direction along the c axis. The gauge-invariant phase difference at ℓth junction is denoted as $\phi(x,y,\ell,t)$. In the region inside the IJJ's the electric and induction fields are descritized as $\vec{E}(x,y,\ell,t)$ and $\vec{B}(x,y,\ell,t)$ along the z direction, where E_z, B_x, and B_y (E_x, E_y, and B_z) are defined on the insulating (superconducting) layers as illustrated in Fig. 1, where the junctions are located in the in-plane regions, $-L_x/2 \leq x \leq L_x/2$ and $-L_y/2 \leq y \leq L_y/2$. We assume that the constant bias current $j_{\rm ext}$ is injected homogeneously in the electrodes attached at $z = \pm L_{jz}/2$.

In this system we have the generalized Josephson relations,

$$\frac{\partial}{\partial t}\phi(x,y,\ell,t) = \frac{2ed}{\hbar}(1-\alpha\Delta_z^2)E_z(x,y,\ell,t), \qquad (2.1)$$

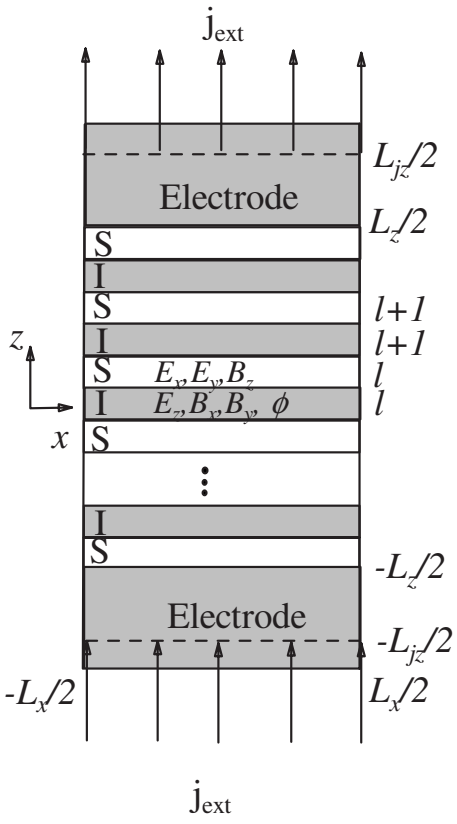

FIG. 1. Schematic view of the intrinsic Josephson junctions covered with normal electrodes. The number ℓ denotes the junction index. The bias current j_{ext} is injected in the c direction.

$$\nabla_x \phi(x,y,\ell,t) = \frac{2ed}{\hbar c}(1-\eta\Delta_z^2)B_y(x,y,\ell,t), \tag{2.2}$$

$$\nabla_y \phi(x,y,\ell,t) = -\frac{2ed}{\hbar c}(1-\eta\Delta_z^2)B_x(x,y,\ell,t), \tag{2.3}$$

where d is the width of the insulating layers, α and η are the interlayer capacitive and inductive coupling constants, respectively, and Δ_z^2 indicates the second-rank difference defined as

$$\Delta_z^2 f(\ell) = f(\ell+1) + f(\ell-1) - 2f(\ell). \tag{2.4}$$

The Maxwell equation for the discrete EM field inside the junctions is given by

$$\frac{1}{c}\frac{\partial}{\partial t}\epsilon E_z(x,y,\ell,t) = \nabla_x B_y(x,y,\ell,t) - \nabla_y B_x(x,y,\ell,t) - \frac{4\pi}{c}[j_c \sin\phi(x,y,\ell,t) + \sigma E_z(x,y,\ell,t)], \tag{2.5}$$

where ϵ and σ are the dielectric constant and the conductivity of the insulating layers, respectively, and j_c is the Josephson critical current density. Note that the EM field components, $E_{x,y}$ and B_z, are neglected in deriving Eqs. (2.2) and (2.3), i.e.,

$$E_{x,y}(x,y,\ell,t) = 0, \tag{2.6}$$

$$B_z(x,y,\ell,t) = 0, \tag{2.7}$$

since the voltage difference in the in-plane direction is usually negligibly small and no external magnetic field is applied.

In the present model the Maxwell equations in the electrodes are assumed as

$$\frac{1}{c}\frac{\partial}{\partial t}\epsilon_L \vec{E}(x,y,z,t) = \vec{\nabla}\times\vec{B}(x,y,z,t) - \frac{4\pi}{c}[\vec{j}_{\text{ext}}(x,y,z) + \sigma_L \vec{E}(x,yz,t)] \tag{2.8}$$

and

$$\frac{1}{c}\frac{\partial}{\partial t}\vec{B}(x,y,z,t) = -\vec{\nabla}\times\vec{E}(x,y,z,t), \tag{2.9}$$

where $j_{\text{ext}}(x,y,z)$ stands for the injected bias current. Since the bias current should be supplied from outside the electrode, we assume the Maxwell equations containing an external current beam in the vacuum region as

$$\frac{1}{c}\frac{\partial}{\partial t}\epsilon_0 \vec{E}(x,y,z,t) = \vec{\nabla}\times\vec{B}(x,y,z,t) - \frac{4\pi}{c}\vec{j}_{\text{ext}}(x,y,z) \tag{2.10}$$

and

$$\frac{1}{c}\frac{\partial}{\partial t}\vec{B}(x,y,z,t) = -\vec{\nabla}\times\vec{E}(x,y,z,t). \tag{2.11}$$

Since Maxwell equations (2.10) and (2.11) are linear, the EM field created by $j_{\text{ext}}(x,y,z)$ can be eliminated from the total EM field by a simple subtraction; that is, the EM wave solution in the vacuum in our model does not depend on the spatial distribution of $j_{\text{ext}}(x,y,z)$. In the following calculations we choose $\vec{j}_{\text{ext}}$ in Eqs. (2.8) and (2.10) as

$$j_{\text{ext}\,x}(x,y,z) = 0, \quad j_{\text{ext}\,y}(x,y,z) = 0, \tag{2.12}$$

$$j_{\text{ext}\,z}(x,y,z) = j_{\text{ext}}\theta(x+L_x/2)\,\theta(L_x/2-x) + \theta(y+L_y/2)\,\theta(L_y/2-y)\,\theta(-L_{Lz}/2-z) \times \theta(z-L_{Lz}/2). \tag{2.13}$$

In the above equations the current $\vec{j}_{\text{ext}}$ is regarded as a homogeneous current (electron) beam. In our simulations the cross section of the beam is assumed to be the same as that of the electrodes, for simplicity. We find $E_z = j_{\text{ext}}/\sigma$ in the case of $\sigma \ll \sigma_L$, irrespective of the value of the cross section of the current beam. By solving those coupled equations simultaneously one can obtain the temporal and spatial variations in the phase difference ϕ and the EM fields $\vec{E}$ and $\vec{B}$. In this paper we perform numerical calculations for two simplified models, xy and xz, which are obtained by reducing the degree of freedom from the above equations as a first step toward the calculations for the full 3D model.

B. Two-dimensional model: *xy* model

In the *xy* model we assume that the system is homogeneous in the z direction (infinite in this direction). In this system the phase difference and the EM field become spatially 2D functions, i.e., $\phi(x,y,t)$, $E_z(x,y,t)$, $B_x(x,y,t)$, and $B_y(x,y,t)$, and the coupling between junctions is effectively inactive. Thus, we find the equations valid inside the junction as

$$\frac{\partial}{\partial t}\phi(x,y,t) = \frac{2ed}{\hbar}E_z(x,y,t), \tag{2.14}$$

$$B_x(x,y,t) = -\frac{\hbar c}{2ed}\nabla_y \phi(x,y,t), \tag{2.15}$$

$$B_y(x,y,t) = \frac{\hbar c}{2ed}\nabla_x \phi(x,y,t), \tag{2.16}$$

$$\frac{1}{c}\frac{\partial}{\partial t}\epsilon E_z(x,y,t) = \nabla_x B_y(x,y,t) - \nabla_y B_x(x,y,t) - \frac{4\pi}{c}[j_c \sin\phi(x,y,t) + \sigma E_z(x,y,t)].$$

$$\frac{1}{c}\frac{\partial}{\partial t}\epsilon E_z(x,y,t) = \nabla_x B_y(x,y,t) - \nabla_y B_x(x,y,t) - \frac{4\pi}{c}[j_c \sin\phi(x,y,t) + \sigma E_z(x,y,t)].$$

(2.17)

In the space outside the IJJ's we have the Maxwell equations in the vacuum,

$$\frac{1}{c}\frac{\partial}{\partial t}\epsilon_0 E_z(x,y,t) = \nabla_x B_y(x,y,t) - \nabla_y B_x(x,y,t), \tag{2.18}$$

and

$$\frac{1}{c}\frac{\partial}{\partial t}B_x(x,y,t) = -\nabla_y E_z(x,y,t),$$

$$\frac{1}{c}\frac{\partial}{\partial t}B_y(x,y,t) = \nabla_x E_z(x,y,t). \tag{2.19}$$

In this model the bias current can be introduced by using the Ampere's law,[21,22]

$$\int_C d\vec{\ell}\cdot\vec{B}_{\rm dc} = \frac{4\pi}{c}j_{\rm ext}L_x L_y, \tag{2.20}$$

where C indicates a counterclockwise contour surrounding the edge of the junction, and the subscript "dc" stands for the dc component.

C. Two-dimensional model: *xz* model

In the *xz* model the spatial variation along the y axis is neglected. As a result, the phase differences and the EM field are reduced to 2D functions as $\phi(x,z,t)$, $E_z(x,z,t)$, $E_x(x,z,t)$, and $B_y(x,z,t)$. Furthermore, we consider only the in-phase motion of the phase differences. In this case the coupling between junctions vanishes. Then, we have the equations valid inside the junction,

$$\frac{\partial}{\partial t}\phi(x,\ell,t) = \frac{2ed}{\hbar}E_z(x,\ell,t), \tag{2.21}$$

$$B_y(x,\ell,t) = \frac{\hbar c}{2ed}\nabla_x \phi(x,\ell,t), \tag{2.22}$$

$$E_x(x,\ell,t) = 0, \tag{2.23}$$

$$\frac{1}{c}\frac{\partial}{\partial t}\epsilon E_z(x,\ell,t) = \nabla_x B_y(x,\ell,t) - \frac{4\pi}{c}[j_c \sin\phi(x,\ell,t) + \sigma E_z(x,\ell,t)].$$

$$\frac{1}{c}\frac{\partial}{\partial t}\epsilon E_z(x,\ell,t) = \nabla_x B_y(x,\ell,t) - \frac{4\pi}{c}[j_c \sin\phi(x,\ell,t) + \sigma E_z(x,\ell,t)].$$

(2.24)

Note that $\phi(x,\ell,t)$, $E(x,\ell,t)$, and $B(x,\ell,t)$ are independent of ℓ since the in-phase motion is assumed. The EM field in the electrodes and in the vacuum is, respectively, described by the set of equations,

$$\frac{1}{c}\frac{\partial}{\partial t}\epsilon_L E_z(x,z,t) = \nabla_x B_y(x,z,t) - \frac{4\pi}{c}[j_{{\rm ext}\,z}(x,z,t) + \sigma_L E_z(x,z,t)], \tag{2.25}$$

$$\frac{1}{c}\frac{\partial}{\partial t}\epsilon_L E_x(x,z,t) = -\nabla_z B_y(x,z,t), \tag{2.26}$$

$$\frac{1}{c}\frac{\partial}{\partial t}B_x(x,z,t) = -\nabla_y E_z(x,z,t), \tag{2.27}$$

$$\frac{1}{c}\frac{\partial}{\partial t}B_y(x,z,t) = \nabla_x E_z(x,z,t), \tag{2.28}$$

and

$$\frac{1}{c}\frac{\partial}{\partial t}\epsilon_0 E_z(x,z,t) = \nabla_x B_y(x,z,t) - \frac{4\pi}{c}j_{{\rm ext}\,z}(x,z,t), \tag{2.29}$$

$$\frac{1}{c}\frac{\partial}{\partial t}\epsilon_0 E_x(x,z,t) = -\nabla_z B_y(x,z,t), \tag{2.30}$$

$$\frac{1}{c}\frac{\partial}{\partial t}B_x(x,z,t) = -\nabla_y E_z(x,z,t), \tag{2.31}$$

$$\frac{1}{c}\frac{\partial}{\partial t}B_y(x,z,t) = \nabla_x E_z(x,z,t). \tag{2.32}$$

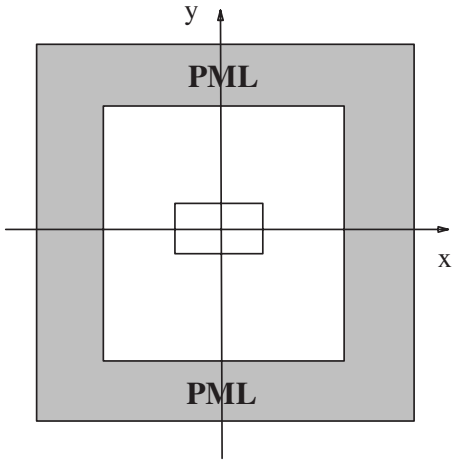

FIG. 2. Schematic view of the *xy* model. The square at the center represents the junction plane located in the vacuum enclosed by PML.

III. SCALED EQUATIONS AND PML

In the numerical calculations we have to solve the coupled equations practically in the *finite* region, though the space surrounding the IJJ's is supposed to extend to infinity. To handle this problem and obtain only *expanding* EM wave solutions, one can utilize the Berenger's method.[29] In this method the equations are solved in the finite region enclosed by the PML (see Figs. 2 and 8). The PML is a fictitious layer which absorbs outgoing EM waves without reflection. To apply this method in the present IJJ's we also have to extract the oscillatory components from the total EM field, which contains dc electric and magnetic field components induced by the constant bias current since the PML should absorb only EM wave components. This procedure is also needed to evaluate the emitted power from the Poynting vector.

Let us first subtract the static component of the magnetic field induced by the constant bias current. For this we introduce an auxiliary field $\vec{B}_0(x,y)$ which satisfies $B_{0z}(x,y)=0$ and

$$\nabla_x B_{0y}(x,y) - \nabla_y B_{0x}(x,y) = \frac{4\pi}{c} j_{\rm ext}(x,y), \tag{3.1}$$

where

$$j_{\rm ext}(x,y) = \theta(x+L_x/2)\,\theta(L_x/2-x)\,\theta(y+L_y/2)\,\theta(L_y/2-y). \tag{3.2}$$

The phase difference $\phi_0(x,y)$ related to $\vec{B}_0$ then satisfies the equation,

$$-(\nabla_x^2+\nabla_y^2)\phi_0(x,y) = \frac{4\pi}{c} j_{\rm ext}(x,y), \tag{3.3}$$

inside the junction. Thus, the solutions can be expressed as

$$\vec{B} = \vec{B}_0 + \vec{b}, \tag{3.4}$$

$$\phi = \phi_0 + \varphi, \tag{3.5}$$

for splitting the oscillatory components.

In the present IJJ's we have the plasma frequency, $\omega_p^2 \equiv 8\pi e d j_c/\hbar\epsilon$, and the *c*-axis penetration depth, $\lambda_c \equiv c/\sqrt{\epsilon}\omega_p$, which give the characteristic scales. One can also define the characteristic EM field in terms of these quantities as $E_p = \hbar\omega_p/2ed$ and $B_c = \hbar c/2ed\lambda_c$ and the dimensionless dissipation constant $\beta = \sigma E_p/j_c$. In the following numerical calculations the time, length, and EM field are normalized in terms of these characteristic quantities.

A. *xy* model

The ac electric field e_z is introduced as

$$e_z = E_z - e_0, \tag{3.6}$$

where e_0 is the static electric field. Coupled equations (2.14)–(2.17) inside the junctions can be rewritten in terms of the ac and dc components of the EM field as

$$\frac{1}{\omega_p}\frac{\partial}{\partial t}\varphi = \frac{e_z+e_0}{E_p}, \tag{3.7}$$

$$\frac{E_x}{E_p} = 0, \tag{3.8}$$

$$\frac{b_x}{B_c} = -\lambda_c \nabla_y \varphi, \tag{3.9}$$

$$\frac{b_y}{B_c} = \lambda_c \nabla_x \varphi, \tag{3.10}$$

$$\frac{1}{\omega_p}\frac{\partial}{\partial t}\frac{e_z}{E_p} = \frac{j_{\rm ext}}{j_c} + \lambda_c \nabla_x \frac{b_y}{B_c} - \lambda_c \nabla_y \frac{b_x}{B_c} - \sin(\phi_0+\varphi) - \beta\frac{e_z+e_0}{E_p}. \tag{3.11}$$

Equations (2.18) and (2.19) in the vacuum is also rewritten as

$$\frac{1}{\omega_p}\frac{\partial}{\partial t}\frac{\epsilon_0}{\epsilon}\frac{e_z}{E_p} = \lambda_c \nabla_x \frac{b_y}{B_c} - \lambda_c \nabla_y \frac{b_x}{B_c}, \tag{3.12}$$

$$\frac{1}{\omega_p}\frac{\partial}{\partial t}\frac{b_x}{B_c} = -\lambda_c \nabla_y \frac{e_z}{E_p}, \tag{3.13}$$

$$\frac{1}{\omega_p}\frac{\partial}{\partial t}\frac{b_y}{B_c} = \lambda_c \nabla_x \frac{e_z}{E_p}. \tag{3.14}$$

The static phase difference ϕ_0 in Eq. (3.11) is obtained by solving Eq. (3.3) as

$$\phi_0 = \left(\frac{j}{4\pi j_c}\right)\Bigg[\left(\frac{x}{\lambda_c}-\frac{L_x}{2\lambda_c}\right)^2\left(\tan^{-1}\frac{\frac{L_y}{2\lambda_c}-\frac{y}{\lambda_c}}{\frac{L_x}{2\lambda_c}-\frac{x}{\lambda_c}}+\tan^{-1}\frac{\frac{y}{\lambda_c}+\frac{L_y}{2\lambda_c}}{\frac{L_x}{2\lambda_c}-x}\right)-\left(y-\frac{L_y}{2\lambda_c}\right)^2\left(-\pi+\tan^{-1}\frac{\frac{L_y}{2\lambda_c}-\frac{y}{\lambda_c}}{\frac{L_x}{2\lambda_c}-\frac{x}{\lambda_c}}+\tan^{-1}\frac{\frac{L_y}{2\lambda_c}-\frac{y}{\lambda_c}}{\frac{x}{\lambda_c}+\frac{L_x}{2\lambda_c}}\right)$$
$$-\left(\frac{x}{\lambda_c}+\frac{L_x}{2\lambda_c}\right)^2\left(-\tan^{-1}\frac{\frac{L_y}{2\lambda_c}-\frac{y}{\lambda_c}}{\frac{x}{\lambda_c}+\frac{L_x}{2\lambda_c}}-\tan^{-1}\frac{\frac{y}{\lambda_c}+\frac{L_y}{2\lambda_c}}{\frac{x}{\lambda_c}+\frac{L_x}{2\lambda_c}}\right)+\left(\frac{y}{\lambda_c}+\frac{L_y}{2\lambda_c}\right)^2\left(-\pi-\tan^{-1}\frac{\frac{y}{\lambda_c}+\frac{L_y}{2\lambda_c}}{\frac{L_x}{2\lambda_c}-\frac{x}{\lambda_c}}-\tan^{-1}\frac{\frac{y}{\lambda_c}+\frac{L_y}{2\lambda_c}}{\frac{x}{\lambda_c}+\frac{L_x}{2\lambda_c}}\right)$$
$$+\left(\frac{x}{\lambda_c}-\frac{L_x}{2\lambda_c}\right)\left(\frac{y}{\lambda_c}-\frac{L_y}{2\lambda_c}\right)\left\{\log\left[\left(\frac{x}{\lambda_c}-\frac{L_x}{2\lambda_c}\right)^2+\left(\frac{y}{\lambda_c}-\frac{L_y}{2\lambda_c}\right)^2\right]-3\right\}-\left(\frac{x}{\lambda_c}+\frac{L_x}{2\lambda_c}\right)\left(\frac{y}{\lambda_c}-\frac{L_y}{2\lambda_c}\right)$$
$$\times\left\{\log\left[\left(\frac{x}{\lambda_c}+\frac{L_x}{2\lambda_c}\right)^2+\left(\frac{y}{\lambda_c}-\frac{L_y}{2\lambda_c}\right)^2\right]-3\right\}-\left(\frac{x}{\lambda_c}-\frac{L_x}{2\lambda_c}\right)\left(\frac{y}{\lambda_c}+\frac{L_y}{2\lambda_c}\right)\left\{\log\left[\left(\frac{x}{\lambda_c}-\frac{L_x}{2\lambda_c}\right)^2+\left(\frac{y}{\lambda_c}+\frac{L_y}{2\lambda_c}\right)^2\right]-3\right\}$$
$$+\left(\frac{x}{\lambda_c}+\frac{L_x}{2\lambda_c}\right)\left(\frac{y}{\lambda_c}+\frac{L_y}{2\lambda_c}\right)\left\{\log\left[\left(\frac{x}{\lambda_c}+\frac{L_x}{2\lambda_c}\right)^2+\left(\frac{y}{\lambda_c}+\frac{L_y}{2\lambda_c}\right)^2\right]-3\right\}\Bigg] \tag{3.15}$$

The dc electric field e_0 in the above equations is determined so as to satisfy the relation,

$$\int_C d\vec{\ell}\cdot\vec{b}_{\rm dc}=0. \tag{3.16}$$

Note that Eq. (3.16) is derived from Eqs. (2.20) and (3.4).

B. *xz* model

Equations (2.21)–(2.32) inside the junction can be rewritten in terms of the ac and dc fields as

$$\frac{1}{\omega_p}\frac{\partial}{\partial t}\varphi=\frac{E_z}{E_p}, \tag{3.17}$$

$$\frac{E_x}{E_p}=0, \tag{3.18}$$

$$b_y/B_c=\lambda_c\nabla_x\varphi, \tag{3.19}$$

$$\frac{1}{\omega_p}\frac{\partial}{\partial t}\frac{E_z}{E_p}=\frac{j_{\rm ext}}{j_c}+\lambda_c\nabla_x\frac{b_y}{B_c}-\sin(\phi_0+\varphi)-\beta\frac{E_z}{E_p}. \tag{3.20}$$

In the outside junction we have

$$\frac{1}{\omega_p}\frac{\partial}{\partial t}\frac{D_x}{E_p}=-\lambda_c\nabla_y\frac{b_y}{B_c}, \tag{3.21}$$

$$\frac{1}{\omega_p}\frac{\partial}{\partial t}\frac{D_z}{E_p}=\lambda_c\nabla_x\frac{b_y}{B_c}-\frac{j}{j_c}, \tag{3.22}$$

$$\frac{1}{\omega_p}\frac{\partial}{\partial t}\frac{b_y}{B_c}=-\lambda_c\nabla_z\frac{E_x}{E_p}+\lambda_c\nabla_x\frac{E_z}{E_p}, \tag{3.23}$$

where

$$D_z=\begin{cases}\dfrac{\epsilon_L}{\epsilon}E_z & \text{in the leads}\\ \dfrac{\epsilon_0}{\epsilon}E_z & \text{in the vacuum}\end{cases} \tag{3.24}$$

and

$$\frac{j}{j_c}=\begin{cases}\beta_L\dfrac{E_z}{E_p}-\dfrac{j_{\rm ext}}{j_c} & \text{in the leads}\\ 0 & \text{in the vacuum}\end{cases}. \tag{3.25}$$

ϕ_0 is given by

$$\phi_0=\frac{1}{2}\frac{j_{\rm ext}}{j_c}x^2 \quad (-L_x/2<x<L_x/2). \tag{3.26}$$

The emitted power is evaluated at the position $\vec{L}_{\rm obs}$ from the time average of the Poynting vector

$$S/S_p=\frac{1}{T}\int_{t_0}^{t_0+T}dt\vec{n}\cdot[\vec{E}(\vec{L}_{\rm obs},t)\times\vec{B}(\vec{L}_{\rm obs},t)]/(E_pB_c), \tag{3.27}$$

where $\vec{n}$ indicate the direction of the observation point and

$$S_p=\frac{c}{4\pi}E_pB_c. \tag{3.28}$$

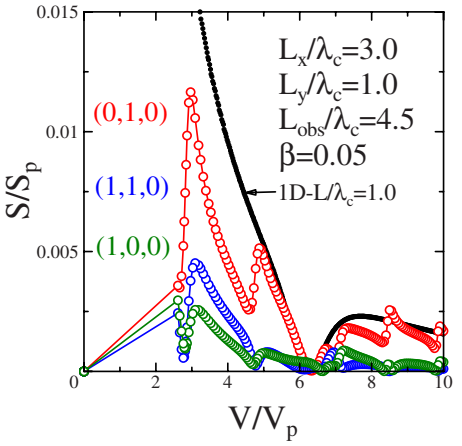

FIG. 3. (Color online) Voltage dependence of the emitted power for $L_x/\lambda_c=3.0$ and $L_y/\lambda_c=1.0$. The red, blue, and green circles express the numerical results for the power observed, respectively, in the (0,1,0), (1,1,0), and (0,1,0) directions. Solid lines between circles are the interpolation. The result for the 1D model of length $L/\lambda_c=1.0$ is also plotted for comparison (small solid circles).

IV. RESULTS OF NUMERICAL CALCULATIONS

A. *xy* model

We solved numerically Eqs. (3.7)–(3.14) in the system shown in Fig. 2. In the following calculations we set the junction size to $L_x/\lambda_c=3.0$ and $L_y/\lambda_c=1.0$, which is close to the size of the mesas used in the experiment since $L_x=300$ μm and $L_y=100$ μm in the case of $\lambda_c=100$ μm.

In our simulations the EM field in the equations given in Sec. III A is defined on the alternate grid points of e_z and $b_{x,y}$ as

$$b_y(x_i,y_j) \quad e_z(x_i+\Delta x/2,y_j) \quad b_x(x_i+\Delta x/2,y_j-\Delta y/2),\cdots, \tag{4.1}$$

with

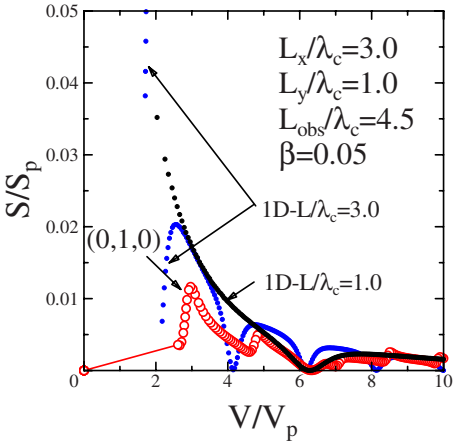

FIG. 4. (Color online) Voltage dependence of the emitted power in the *xy* model (red circles) and 1D models of two different lengths: $L_x/\lambda_c=1.0$ (black circles) and $L_x/\lambda_c=3.0$ (blue circles).

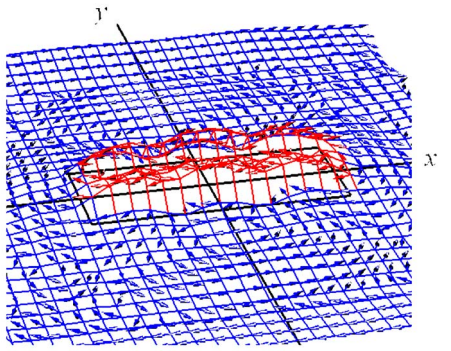

(a) $j_{ext}/j_c=0.39(V/V_p=6.00)$

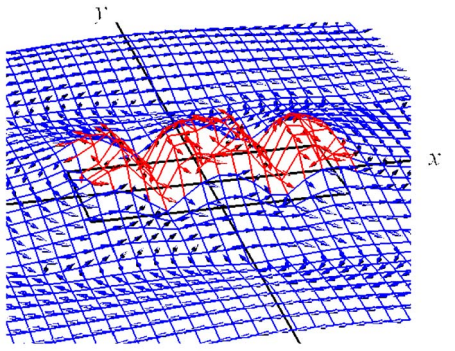

(b) $j_{ext}/j_c=0.25(V/V_p=4.97)$

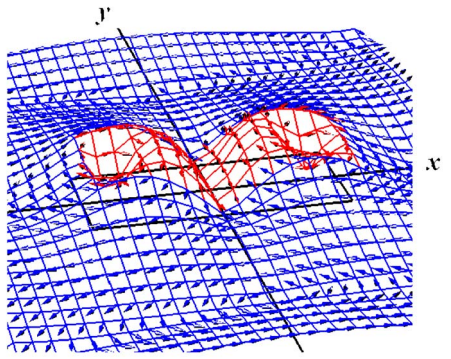

(c) $j_{ext}/j_c=0.175(V/V_p=3.25)$

FIG. 5. (Color online) Spatial distribution of $\vec{b}$ for various bias currents at a certain time. The magnitude $|\vec{b}|$ is given by the vertical coordinate, and its direction is indicated by arrows. The red and blue regions correspond to the inside and the outside junctions.

$$x_i=\Delta x i, \quad y_i=\Delta y j, \tag{4.2}$$

on the basis of the finite difference time domain (FDTD). In this method the grid is formed in such a way that $b_{x,y}$ has a value on every grid point on the boundaries. The spatial derivatives for the EM fields are evaluated, using the midpoint method. For the time derivative we use the fourth-order Runge-Kutta method to obtain stable time development in the present nonlinear system.

Let us now present our numerical results. Figure 3 shows

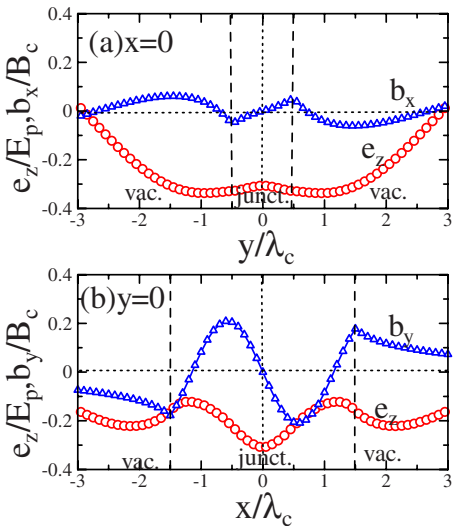

FIG. 6. (Color online) Spatial dependence of the EM field, e_z and b_z, along the (a) y direction at $x=0$ and the (b) x direction at $y=0$ in both regions inside and outside the junctions. The dashed lines indicate the positions of the junction edges.

the voltage dependence of the emitted power at several points in the vacuum, which are situated at a distance $|\vec{L}_{\rm obs}|/\lambda_c=4.5$ from the center of the junction. These points are located, respectively, in the (0,1,0), (1,1,0), and (0,1,0) directions. The strongest emission takes place in the (0,1,0) direction. This result comes from the fact that the (0,1,0) surface of the junctions has a maximum area. We also find that there are several nodes at which the power takes minimum values in the voltage dependence. The analysis for the EM field excited inside the junctions indicates that the spatial pattern of the EM modes changes at these node voltages (see also Fig. 5). The result for the 1D model[21,22] with a length $L/\lambda_c=1.0$ is also plotted in this figure. It is seen that the power emitted in the (0,1,0) direction is nearly equal to that in the 1D model in the high-voltage region. This result indicates that the resonance in this voltage region is subject to

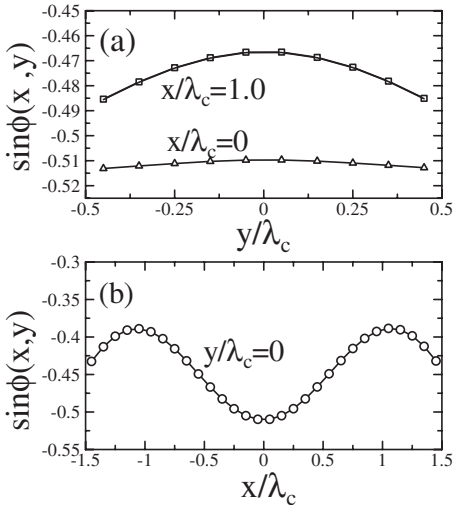

FIG. 7. Spatial dependence of the Josephson current in the (a) y and (b) x directions.

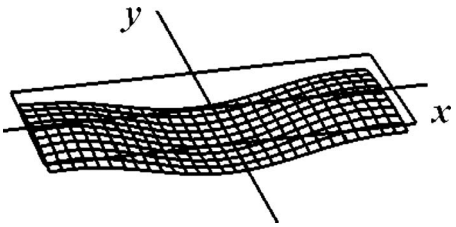

FIG. 8. Two-dimensional view of the Josephson current distribution.

the shorter side ($L_x/\lambda_c=1.0$) of the rectangular junctions.

In Fig. 4 we also compare the result for the (0,1,0) direction with that in the 1D model of length $L=3\lambda_c$, which is equal to that of the longer side of the rectangular junctions. As seen in this figure, the node voltages in the xy model are similar to those in the 1D model with $L/\lambda_c=3.0$. This result comes from the fact that the spatial pattern of the EM field inside the junctions has nodes that are parallel to the shorter side of the junctions (see Fig. 5); that is, the 1D character of the excited EM field appears along the longer side of the junctions. In long 1D Josephson junctions a solitonic mode induced by the parametric excitations appears at half the voltage at which the cavity resonance mode is excited; i.e., $V/V_p=1.5$ in the case of $L/\lambda_c=3.0$. However, this mode does not appear in the xy model; that is, the solitonic excitation modes become unstable in the 2D model.

In Fig. 5, we depict snapshots of the spatial distribution of the induction field $\vec{b}$ at three different voltage (bias current) values. The coordinate in the vertical direction represents the magnitude of $\vec{b}$, and the arrows indicate its directions. Figure 5(a) shows a field pattern at a voltage near the minimum of the power given in Fig. 3. The field patterns near the two peaks in the S vs V curve are presented in Figs. 5(b) and 5(c). From these figures one understands that the flux lines form closed loops extending outside the junctions and have several nodes inside the junctions. In Fig. 5(a) we see that the flux lines seem to penetrate parallel to the longer side of the junction. In this case the emitted power takes a minimum value. This result is understood from the fact that the induction field has nodes at the junction edges parallel to the y

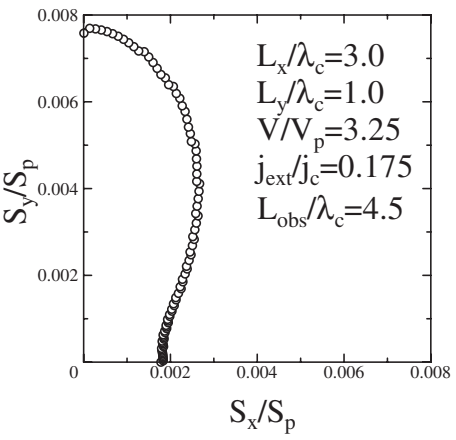

FIG. 9. Angle dependence of the emitted power in the xy model for $j_{\rm ext}/j_c=0.175$ ($V/V_p=3.25$).

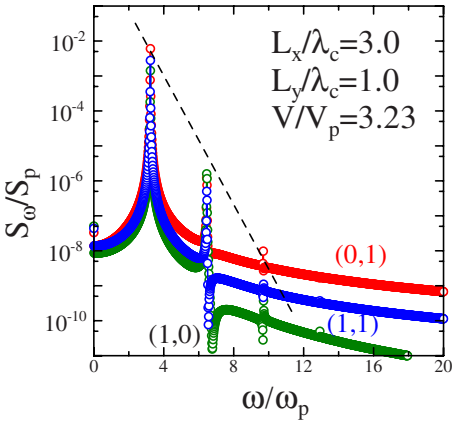

FIG. 10. (Color online) Frequency spectrum of the emitted power in the xy model for $j_{ext}/j_c=0.175$ ($V/V_p=3.25$).

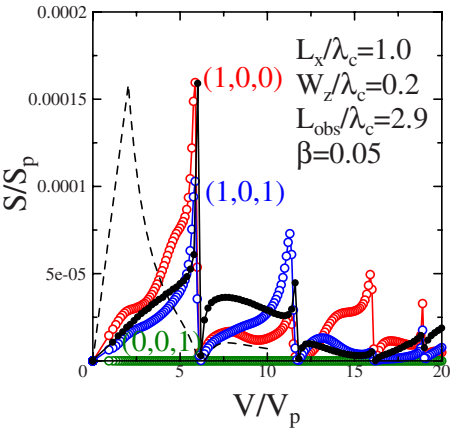

FIG. 12. (Color online) Voltage dependence of the power emitted from the junction with $L_x/\lambda_c=1.0$ and $W_z/\lambda_c=0.2$. The results for the junction with $W_z/\lambda_c=0.02$ (black solid circles) and the 1D model with $L/\lambda_c=1.0$ (dashed line) are also shown in this figure. The results for latter two systems are normalized in such a way that the maximum peak values coincide with each other.

axis. In Figs. 5(b) and 5(c) we find that nodes appear parallel to the shorter side and, as a result, the flux lines inside the junction are mostly parallel to the shorter side. Since the strong emission occurs in these cases, the field patterns given in Figs. 5(b) and 5(c) reveal the eigenmodes of the EM field relevant to the THz emission in the rectangular Josephson junction, which can be excited by the Josephson oscillations. It is also seen that the components giving the complex field pattern rapidly vanish in the near field region and only the EM wave components expanding concentrically can reach the far field region. From our numerical results the total power of emitted EM waves can be estimated. In the case shown in Fig. 5(c) we have 44.4 mW for a mesa of 100 $\times 300 \times 1$ μm^3, which is promising for practical applications.

In order to see the symmetry of the excited EM field distribution, we plot the spatial variation of e_z and b_z along the x and y axes in Figs. 6(a) and 6(b) in the case shown in Fig. 5(c). In both directions the electric (magnetic) field shows symmetric (antisymmetric) distribution, which is similar to an ac EM field in a capacitor.[28] We mention that electric charges appear in the superconducting layers in our solutions, which brings about a resemblance to the field distribution in a capacitor. In the open cavity model in the antenna theory, which is often used in an analysis of the EM waves emitted from a thin plate antenna, which resembles the mesa IJJ's in shape, the metallic plates forming a cavity in the antenna are assumed not to be charged. In such a

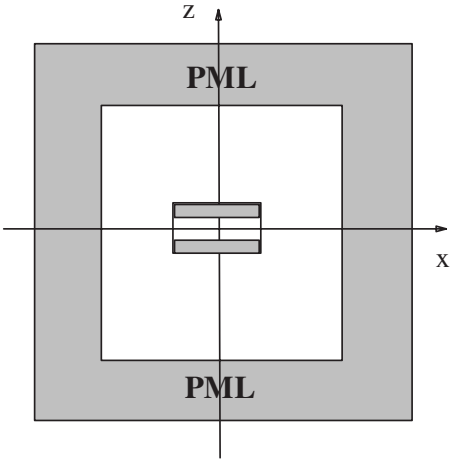

FIG. 11. Schematic view of the xz model. The rectangle at the center represents the junction covered with normal electrodes.

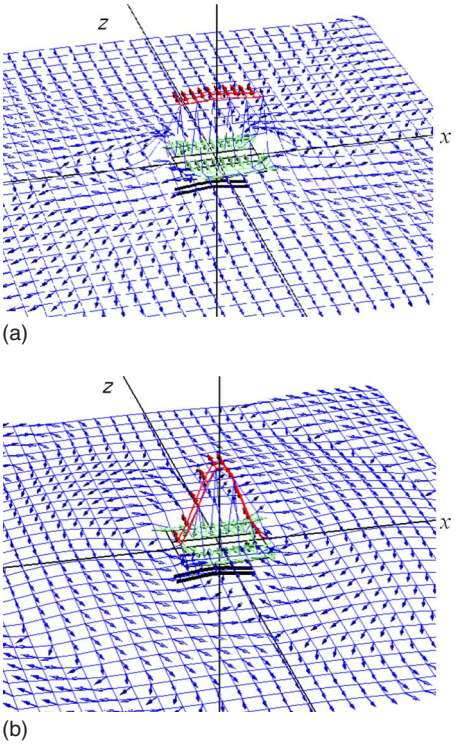

FIG. 13. (Color online) Spatial distribution of (a) the total electronic field $\vec{E}$ and (b) the oscillatory part $\vec{e}$ for $I/I_c=0.293$ ($=V/V_p=5.83$). The magnitudes $|\vec{E}|$ and $|\vec{e}|$ are taken in the vertical direction, and the arrows indicate their directions. The red, blue, and green lines and arrows represent the electric field inside and outside the junctions and inside the electrodes, respectively. The bold black lines show the Josephson current $\sin\phi$.

system the electric (magnetic) field has an antisymmetric (symmetric) pattern. We also plot the spatial dependence of the Josephson current along the x and y axes in Fig. 7. This figure indicates that the oscillating Josephson current has spatially uniform and standing-wave components both. The two-dimensional view of the Josephson current distribution in this case is presented in Fig. 8.

In Fig. 9 the angle dependence of the emitted power is plotted at $j_{\rm ext}/j_c=0.175$ $(=V/V_p=3.15)$, where the emission is strongest. As seen in this figure, the strong emission occurs in the y direction, though the EM wave is emitted in all the directions. The frequency spectrum of the emitted power in this case is shown in Fig. 10. One can see that the emitted EM wave is coherent and its fundamental mode has the Josephson frequency. The intensity of the higher harmonics decreases, following the inverse square law.

B. *xz* model

Let us present numerical results for the EM wave emission in the xz model (see Fig. 11). In our simulations the length L_x and the thickness W_z of the junction are chosen as $L_x/\lambda_c=1.0$ and $W_z/\lambda_c=0.2$ and the width of the electrodes attached on both sides of the junction is set to $W_{\rm el}/\lambda_c=0.2$.

Figure 12 shows the voltage dependence of the power emitted in three directions: (1,0,0), (1,0,1), and (0,0,1). It is seen that the sharp peaks appear at several voltage values and the emission is the strongest in the (1,0,0) direction. In this figure we also plot the power emitted from a thinner junction with $W_z/\lambda_c=0.02$ in the (1,0.0) direction (black circles). It is noted that the node voltages do not depend on the width W_z, but the shape of the voltage dependence changes and the peaks become sharper when the width of the junction is reduced.

Figure 13 shows snapshots of the spatial distribution of the electric field at a voltage $V/V_p=5.83$ $(j/j_c=0.293)$ near one of the peaks. The electric field contains a large dc component which decreases rapidly in the vacuum outside the junction as seen in Fig. 13(a). In Fig. 13(b) we plot the oscillating component $\vec{e}$ $(=\vec{E}-\vec{E}_{\rm stat})$, subtracting the dc component $\vec{E}_{\rm stat}$ from $\vec{E}$. Note that the pattern of the expanding EM wave shown in this figure is very similar to that in the dipole emission. We plot the angle dependence of the emitted power at $V/V_p=5.83$ $(j/j_c=0.293)$ in Fig. 14. This figure reveals that the emission in this model can really be regarded as the dipole emission, whose angle dependence is given by $S\propto \sin^2\theta$, with θ being the angle from the z axis. This result comes from the fact that alternating electric charges appear in the electrodes in the xz model, which look like dipole charges. Thus, one understands that the xy model is analogous to the dipole antenna. The total power emitted in this case is estimated to be 4.3 mW. This value is similar to the one estimated in the xy model.

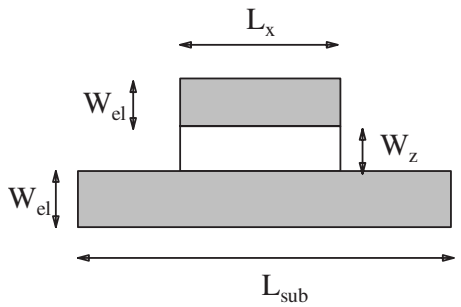

FIG. 15. Illustration of the junction with asymmetric electrodes in the xz model. The sizes of the junction and the electrodes are taken as $L_x/\lambda_c=1.0$, $W_z/\lambda_c=0.2$, $L_{\rm sub}/\lambda_c=3.0$, and $W_{\rm el}/\lambda_c=0.2$.

The distribution of the emitted EM waves is also affected by the environment around the junctions. To see this, we also perform the simulations for the junction system in which the lower electrode is longer than the upper one as shown in Fig. 15. The direction in which the strongest emission is observed is rotated by 45° from the lower electrode surface as seen in Fig. 16. This result indicates that the emitted EM wave is reflected by the lower electrode surface. As a result, the voltage dependence of the emitted power is also affected by the reflection as shown in Fig. 16.

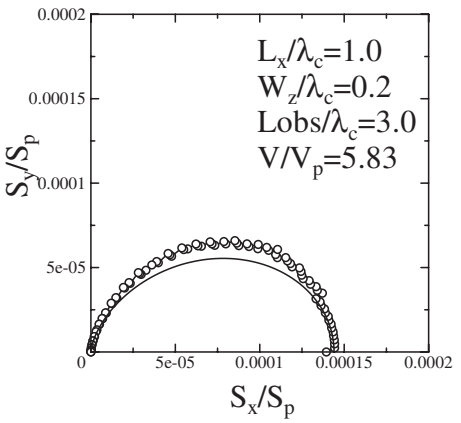

FIG. 14. Angle dependence of the emitted power in the xz model for $I/I_c=0.293$ $(V/V_p=5.83)$ (black circles). The power distribution in the dipole emission is also shown for comparison (solid line).

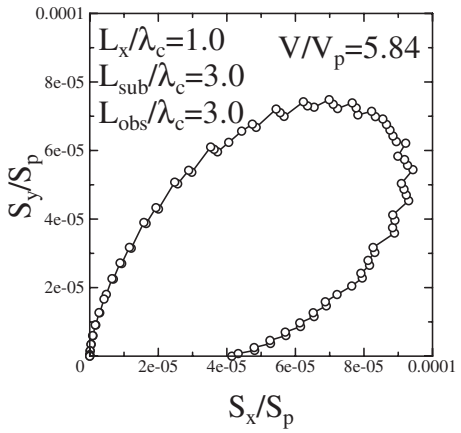

FIG. 16. Angle dependence of the emitted power in the xz model for $I/I_c=0.293$ $(V/V_p=5.83)$.

V. CONCLUDING REMARKS

In this paper we investigated the EM wave emission from the IJJ's, using the *xy* and *xz* models. On the basis of these models we discussed the EM excitation modes in the 2D extended junctions, the distribution of the emitted EM waves, and the effect of electrodes (substrate) attached on the top and bottom junctions. In our models the Maxwell equations are directly solved in both regions inside and outside the junctions so that the EM wave emission from the junction edges and also the recoil effect on the dynamics of the phase differences due to the emission can be accurately described since the correct boundary condition for the EM field is used at the junction edges. The characteristics of the emitted EM waves can also be clarified in our models. Our calculation was able to obtain the EM field in the entire space composed of the IJJ's and the outside vacuum. It is possible to calculate the power distribution of the EM waves emitted from IJJ's devises with arbitrary shape in our method; that is, our numerical method will be applied for designs of IJJ's THz devises.

In the *xy* model we see that the EM wave is emitted from all the junction edges and the power observed becomes maximum in the direction perpendicular to the longer side of the rectangular junctions. It was shown that flux loops penetrate into the extended junctions in the presence of a bias current under no external magnetic field. These flux lines oscillate with the Josephson frequency and emit EM waves. The emitted EM waves are coherent and have the Josephson frequency. The pattern of the emitted EM waves in this model is consistent with the in-plane angle dependence of the power observed in recent experiment.[30]

In the *xz* model we have shown that the spatial pattern of the EM waves emitted from the junctions is similar to that in the dipole emission; that is, the strong emission takes place in the *x* direction. This result indicates that the oscillating EM field inside the junctions is analogous to that in a capacitor under an oscillating bias current. In the dipole emission we have no emitted power in the *z* direction. However, the recent experiment reported that the power takes a minimum value but does not vanish in the *z* direction.[30] This result indicates that the EM field excited inside the junctions has weak spatially asymmetric components too, which might be excited in multijunction systems. In this paper we considered only the in-phase motion of the phase differences. In the IJJ's vortex-antivortex pairs will be excited without an external magnetic field in the voltage state. Since the size of a Josephson vortex in the IJJ's is on the order of $\lambda_J=\lambda_c/\sqrt{\eta}$, which is much less than λ_c and also the size of mesas in which the EM wave emission is observed, it will be possible that traveling (solitonic) modes of vortex-antivortex pairs that induce asymmetric components in the EM field are excited. In the emission from such states the power flowing in the *z* direction may not vanish. The stability of the in-phase motion against the excitation of fluxon loops (vortex-antivortex pairs) in a stack of extended intrinsic Josephson junctions is an interesting future problem.

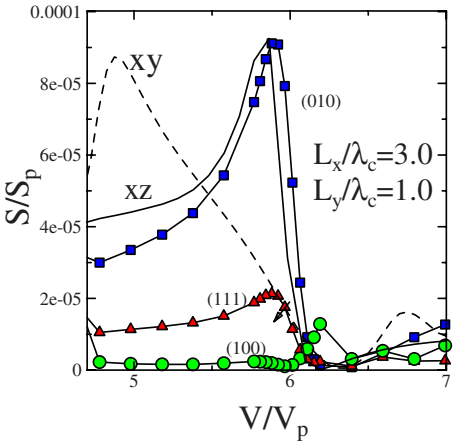

FIG. 17. (Color online) Voltage dependence of the emitted power in the 3D case. For comparison the results for the *xy* model (dotted line) and *xz* model (solid line) are also plotted. The peak values in the latter two models are scaled so as to give the same value as in the 3D system.

The symmetry of the EM field excited in the IJJ's which is relevant to the THz emission in our present calculations is different from that given in Refs. 24 and 25. In our model the spatially symmetric electric field is excited inside the IJJ's in the voltage state causing the THz emission, whereas the excited electric field proposed in Refs. 24 and 25 is antisymmetric and also includes solitonic components. The spatial and temporal variations in the EM field excited inside the IJJ's may be checked by measuring the power distribution of the emitted EM waves. We stress that the effect of device shape should be incorporated into the calculations of the emitted EM waves for comparison with experiments since the power distribution of the EM waves is sensitive to the shape of the electrodes as shown in this paper.

Finally, we briefly mention our preliminary result for the emission in the 3D model (*xyz* model). Figure 17 shows the voltage dependence of the emitted power in the high-voltage region. In this figure we also plot the power obtained in the *xy* and *xz* models for comparison in the scale in which the peak values coincide with each other. As seen in this figure, the position of the node coincides in these three models and the peaks generally become sharper in the 3D model. It is also noted that the sharp increase in the power along the (010) direction just below the node voltage is similar to that in the *xz* model. One may also see that the power emitted in the (111) direction has some resemblance with that in the *xy* model near the node voltage. From this result one understands that the calculated results obtained in the *xy* and *xz* models reflect some features in the realistic 3D model.

ACKNOWLEDGMENTS

One of the authors (H.M.) thanks N. Toyota for useful discussions. This work was supported partially by Grant-in-Aid for Scientific Research on Priority Area and JSPS Core-to-Core Program Strategic Research Networks NES.

*tkoyama@imr.tohoku.ac.jp
†matumoto@ldp.phys.tohoku.ac.jp
‡machida.masahiko@jaea.go.jp
§kadowaki@ims.tsukuba.ac.jp

[1] T. Koyama and M. Tachiki, Phys. Rev. B **54**, 16183 (1996).
[2] M. Machida, T. Koyama, and M. Tachiki, Phys. Rev. Lett. **83**, 4618 (1999).
[3] H. Matsumoto, S. Sakamoto, F. Wajima, T. Koyama, and M. Machida, Phys. Rev. B **60**, 3666 (1999).
[4] R. Kleiner, F. Steinmeyer, G. Kunkel, and P. Muller, Phys. Rev. Lett. **68**, 2394 (1992).
[5] M. Itoh, S. I. Karimoto, K. Namekawa, and M. Suzuki, Phys. Rev. B **55**, R12001 (1997).
[6] M. Tachiki, T. Koyama, and S. Takahashi, Phys. Rev. B **50**, 7065 (1994).
[7] T. Koyama and M. Tachiki, Solid State Commun. **96**, 367 (1995).
[8] S. E. Shafranjuk and M. Tachiki, Phys. Rev. B **59**, 14087 (1999).
[9] M. Machida, T. Koyama, A. Tanaka, and M. Tachiki, Physica C **330**, 85 (2000).
[10] M. Machida, T. Koyama, and M. Tachiki, Physica C **362**, 16 (2001).
[11] M. Tachiki, M. Iizuka, K. Minami, S. Tejima, and H. Nakamura, Phys. Rev. B **71**, 134515 (2005).
[12] H. Matsumoto, Physica C **437-438**, 199 (2006).
[13] L. N. Bulaevskii and A. E. Koshelev, Phys. Rev. Lett. **99**, 057002 (2007).
[14] G. Hechtfischer, R. Kleiner, A. V. Ustinov, and P. Muller, Phys. Rev. Lett. **79**, 1365 (1997).
[15] K. Lee, W. Wang, I. Iguchi, M. Tachiki, K. Hirata, and T. Mochiku, Phys. Rev. B **61**, 3616 (2000).
[16] K. Kadowaki, I. Kakeya, T. Yamamoto, T. Yamazaki, M. Kohri, and Y. Kubo, Physica C **437-438**, 111 (2006).
[17] M. H. Bae, H. J. Lee, and J. H. Choi, Phys. Rev. Lett. **98**, 027002 (2007).
[18] L. Ozyuzer *et al.*, Science **318**, 1291 (2007).
[19] I. K. Yanson, V. M. Svistunov, and I. M. Dmitrenko, Sov. Phys. JETP **21**, 650 (1965).
[20] D. N. Langenberg, D. J. Scalapino, B. N. Taylor, and R. E. Eck, Phys. Rev. Lett. **15**, 294 (1965).
[21] H. Matsumoto, T. Koyama, and M. Machida, Physica C **468**, 654 (2008).
[22] H. Matsumoto, T. Koyama, and M. Machida, Physica C **468**, 1899 (2008).
[23] T. A. Fulton and R. C. Dynes, Solid State Commun. **12**, 57 (1973).
[24] A. E. Koshelev, Phys. Rev. B **78**, 174509 (2008).
[25] X. Hu and S. Lin, Phys. Rev. B **78**, 134510 (2008).
[26] C. A. Balanis, *Antenna Theory: Analysis and Design* (John Wiley and Sons Inc., New York, 1997), p. 736.
[27] M. Leone, IEEE Trans. Electromagn. Compat. **45**, 486 (2003).
[28] R. P. Feynman, R. B. Leighton, and M. Sansa, *The Feynman Lectures on Physics-Mainly Electromagnetism and Matter* (Addison-Wesley, Reading, MA, 1964), pp. 23–1.
[29] J. P. Berenger, J. Comput. Phys. **114**, 185 (1994).
[30] K. Kadowaki (unpublished).